INTERNATIONAL JOURNAL FOR NUMERICAL METHODS IN FLUIDS, VOL. 8, 463–474 (1988)

A NAVIER–STOKES CODE FOR S-SHAPED DIFFUSERS—A REVIEW

ALBERT L. LOEFFLER, JR.

Grumman Corporate Research Center, Bethpage NY 11714-3580, U.S.A.

SUMMARY

Three-dimensional, compressible, internal flow solutions obtained using a thin-layer Navier–Stokes code are presented. The code, formulated by P.D. Thomas, is based on the Beam–Warming implicit factorization scheme; the boundary conditions also are formulated implicitly. Turbulent flow is treated through the use of the Baldwin–Lomax two-layer, algebraic eddy viscosity model. Steady-state solutions are obtained by solving numerically the time-dependent equations from given initial conditions until the time-dependent terms become negligible. The configuration considered is a rectangular cross-section, S-shaped centreline diffuser duct with an exit/inlet area ratio of 2·25. The Mach number at the duct entrance is 0·9, with a Reynolds number of $5{\cdot}82 \times 10^5$. Convergence to the final results required about 2700 time steps or 11 hours of CPU time on our CRAY-1M computer. The averaged residuals were reduced by about two orders of magnitude during the computations. Several regions of separated flow exist within the diffuser. The separated flow region on the upper wall, downstream of the second bend, is by far the largest and extends to the exit plane.

KEY WORDS Viscous Turbulent Subsonic Duct Diffuser Navier–Stokes

INTRODUCTON

In the past decade numerous schemes have arisen for solving the Navier–Stokes equations or approximations to these equations. Most of these methods have been for external flows. For application to propulsive systems, however, internal and combination internal–external flows are of paramount importance but, so far, little work has been done in solving the Navier–Stokes equations for this class of problem.[1] The work that has been done is mostly for simple duct geometries, and much of it has been for parabolized equations, thereby ruling out possibilities of flow separation.[2] It is the purpose of this paper to examine the application of a 'thin-layer' approximated Navier–Stokes code to a complex three-dimensional internal flow—namely, an S-shaped, rectangular cross-section diffuser flow. The equations used in this code retain all terms important in boundary layers, both separated and attached, and the code should therefore be able to handle flow separation.

DESCRIPTION OF CODE

The Navier–Stokes code used in this work was formulated by P. D. Thomas.[3–5] It is based on the Beam–Warming[6] implicit factorization scheme. The boundary conditions also are formulated in an implicit fashion consistent with the implicit difference equations for interior grid points. An elliptic grid generation technique is used to construct a boundary-conforming curvilinear co-

© 1987 by Grumman Aerospace Corporation
All Rights Reserved, Published by John Wiley & Sons Limited with permission.

Received 1 December 1986
Revised 24 May 1987

ordinate system. The co-ordinate grid has been suitably stretched near the solid boundaries where large gradients require more computational accuracy. Turbulent flow is treated through the use of a two-layer eddy viscosity model employing a simplified Baldwin–Lomax[7] algebraic turbulence model. Steady-state solutions are obtained by solving numerically the time-dependent equations from given initial conditions until the time-dependent terms become negligible. Due to the implicit treatment of equations and boundary conditions, the code is unconditionally stable with respect to the time-step size. Both explicit smoothing terms and implicit artificial dissipation terms are included in the equations to improve the stability and convergence characteristics. The viscous transport processes in the streamwise direction have been neglected in the equations used in this code. However, the equations still retain all terms that are significant in boundary layers, whether attached or separated.

DESCRIPTION OF DIFFUSER

The configuration considered is a rectangular cross-section, S-shaped centreline diffuser duct. The side walls are parallel and 4·5 inches apart. At the entrance the height is 2 inches, while at the exit the height has increased to 4·5 inches. The area ratio of the diffuser is 2·25. Since the cross-sectional width is constant, this area ratio is accounted for entirely by the increase in the cross-sectional height; the exit cross-section is square. The centreline is formed from two tangential circular arcs; the radius of curvature of the upstream bend is 2·5 inches, while that of the downstream bend is 11·84 inches. The portion of the diffuser duct length having a curved centreline is 10·88 inches. Additional short lengths of 4·0 and 6·65 inches of constant cross-section are attached at the diffuser entrance and exit respectively to give an overall duct length of 21·53 inches; the total length measured along the centreline is 23·0 inches.

BOUNDARY AND INITIAL CONDITIONS

For the present diffuser duct flow, the stagnation enthalpy, the stagnation pressure and the direction cosines of the velocity vector are prescribed at the entrance, whereas at the perimeter of the exit the freestream pressure is specified. This latter condition is used in place of the energy equation. At the diffuser internal walls the velocity must vanish and the adiabatic wall condition is applied to the energy equation. Since the curvature of the diffuser centreline occurs in a vertical plane, there is a vertical plane of symmetry through the centreline of the diffuser and only one half of the diffuser duct cross-section need be considered in the computations. The initial (time = 0) flow consists of an inviscid core flow with a turbulent boundary layer flow at the walls. The Mach number at the duct entrance is 0·9, with a Reynolds number of $5{\cdot}82 \times 10^5$.

RESULTS AND DISCUSSION

The graphical results presented in Figures 1–7 are for the symmetry plane of the diffuser formed by the intersection of the diffuser with a vertical plane through the centreline. The co-ordinate grid in this symmetry plane is shown in Figure 1. The grid lines in computational space in the flow direction are identified by the index J, with J varying from 1 at the entrance plane to 46 at the exit plane. In the transverse planes (perpendicular to the centreline) the indices K and L are used to denote the computational space grid lines in the horizontal and vertical directions respectively. The variation of K is from 1 (symmetry plane) to 15 (side wall) and L varies from 1 (bottom wall) to 29 (top wall). The centreline is located at $K = 1$ and $L = 15$, while $K = 1$ identifies the symmetry plane. The grid spacing is uniform in the flow direction except for the entrance region. Grid stretching

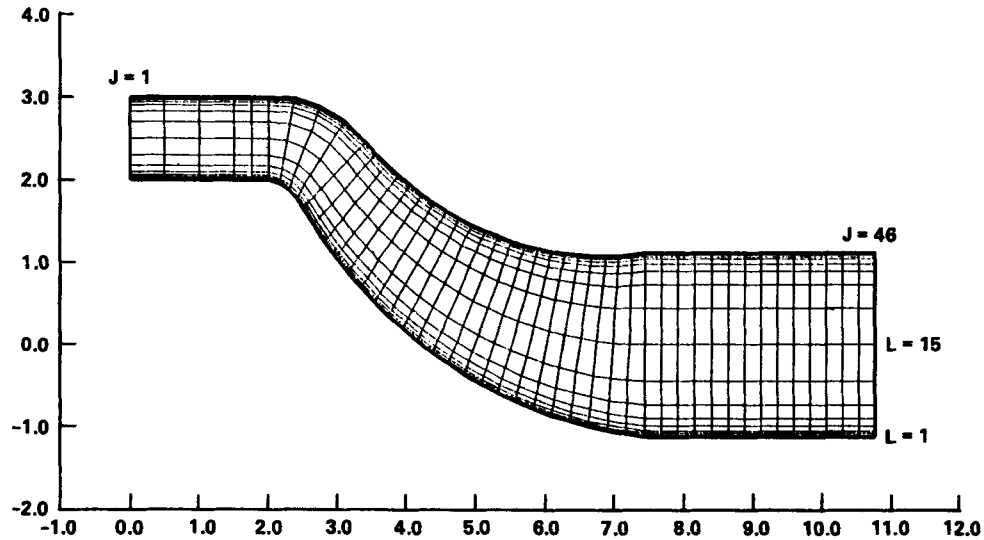

Figure 1. Computational grid in symmetry plane (vertical plane, $K = 1$, through the centreline)

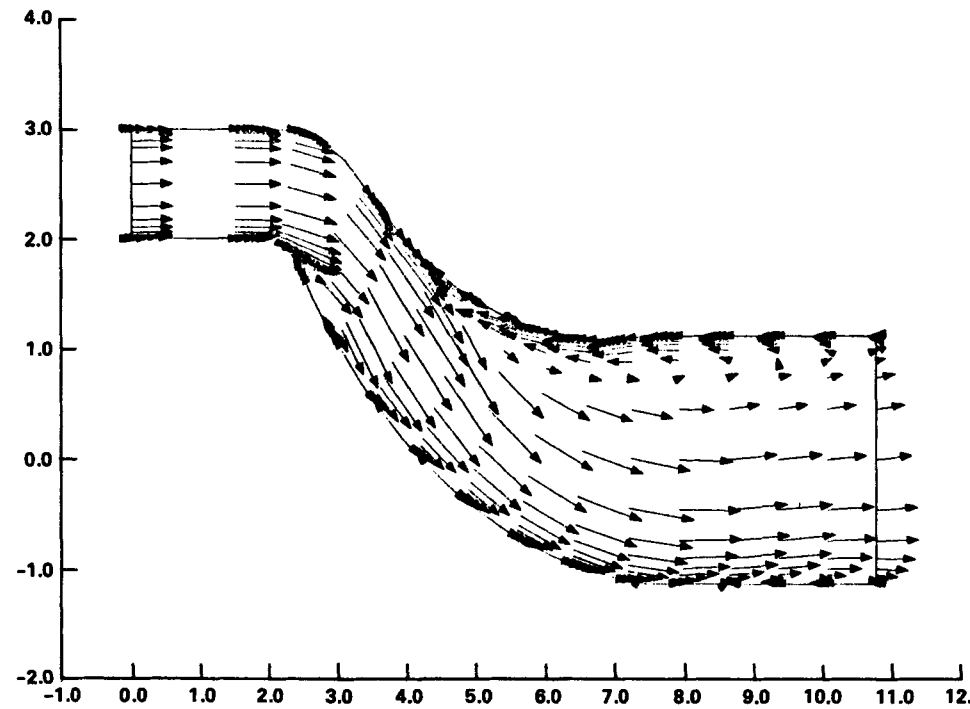

Figure 2. Longitudinal velocity profiles at various axial stations in symmetry plane

was employed in the vertical and horizontal co-ordinate grids, with the grid spacing near the walls of the order of the viscous sublayer thickness.

The velocity profiles at various axial stations are shown in Figure 2. The lengths of the arrows are proportional to the velocity magnitudes. The entrance flow is seen to be uniform except for the

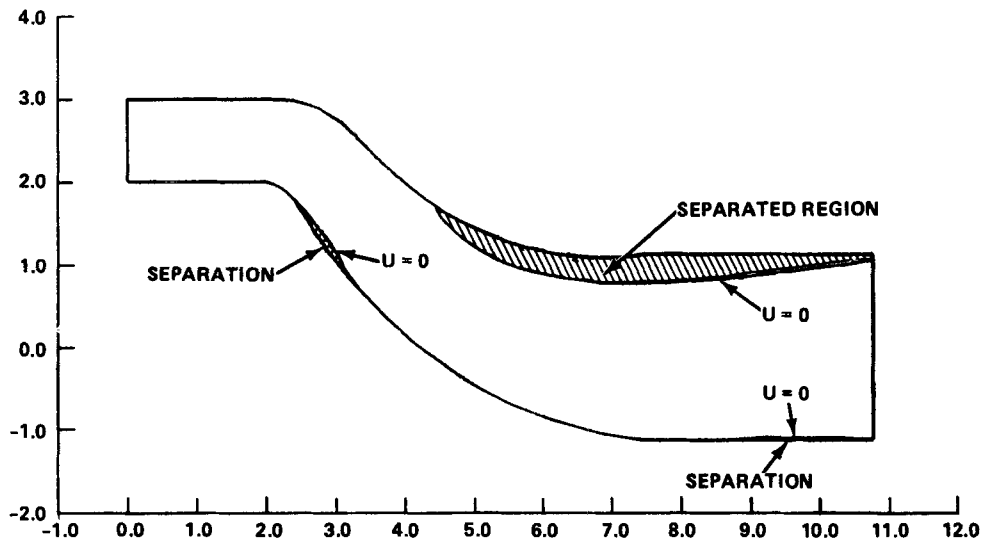

Figure 3. Separated flow regions in symmetry plane

boundary layer regions on the top and bottom walls. Downstream of the first bend on the lower wall and downstream of the second bend on the upper wall, separated flow zones exist. These can be easily identified by the reversed direction of the arrowheads.

The extent of the separated flow regions can be examined much more conveniently in the U-contour plot in Figure 3. U is the horizontal component of longitudinal velocity, made dimensionless with the speed of sound at stagnation conditions. The outer boundaries of the separated flows are given by the contour lines for $U = 0$, while the other contour lines within the separated flow are for negative values of U. The separated flow region on the upper wall is seen to be by far the larger, extending right to the exit plane.

In Figure 4 the U-contours are plotted for the entire range of U, both positive and negative. The value of U is seen to attain a maximum near the lower wall at the second bend of the diffuser. The variation of U throughout the diffuser is quite smooth.

Figure 5 shows the W-contours. W is the vertical component of the longitudinal velocity, made dimensionless with the speed of sound at stagnation conditions. The maximum value of W is seen to occur shortly downstream of the first bend in the diffuser. This is consistent with physical reasoning, since the angle from the horizontal of the diffuser centreline is a maximum in this region. As expected, there is little variation in W at the entrance and exit sections, since W at these points is near zero.

Figure 6 depicts the variation in static pressure in the symmetry plane. The isobars indicate uniform entrance flow, but with considerable pressure disturbances in the vicinity of the channel bends. In the turning portions of the flow many of the isobars exhibit a partial alignment with the flow direction, as would be expected for a pressure field in approximate equilibrium with centrifugal forces. Towards the end of the second bend the flow straightens out and the exit flow is fairly uniform. This observation is consistent with the velocity profiles in Figure 2.

The density contours in Figure 7 largely reflect the static pressure contours shown in Figure 6, because the temperature variations within the difffuser are relatively small.

Figures 1–7 show flow conditions along a vertical plane through the centreline, but give no indication of how the flow properties vary laterally. To visualize lateral variations, we utilize cross-

CONTOUR NO.	U	CONTOUR NO.	U	CONTOUR NO.	U	CONTOUR NO.	U
1	-.9420	6	-.3811	11	.1799	16	.7408
2	-.8298	7	-.2689	12	.2920	17	.8530
3	-.7176	8	-.1567	13	.4042	18	.9652
4	-.6054	9	-.0445	14	.5164	19	1.0773
5	-.4933	10	.0677	15	.6286	20	1.1895

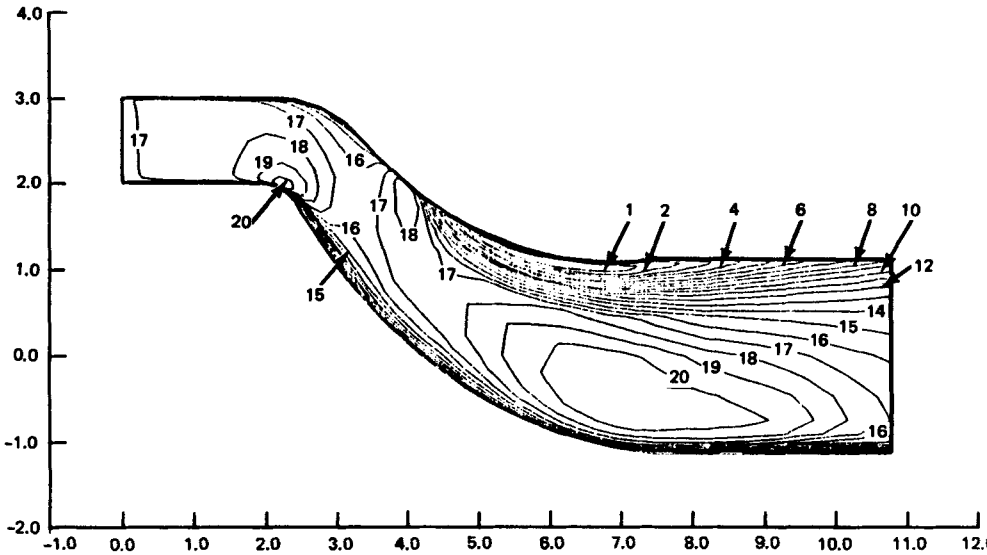

Figure 4. *U*-contours (dimensionless) in symmetry plane

CONTOUR NO.	W	CONTOUR NO.	W	CONTOUR NO.	W	CONTOUR NO.	W
1	-.9138	6	-.5363	11	-.1588	16	.2187
2	-.8383	7	-.4608	12	-.0833	17	.2941
3	-.7628	8	-.3853	13	-.0078		
4	-.6873	9	-.3098	14	.0677		
5	-.6118	10	-.2343	15	.1432		

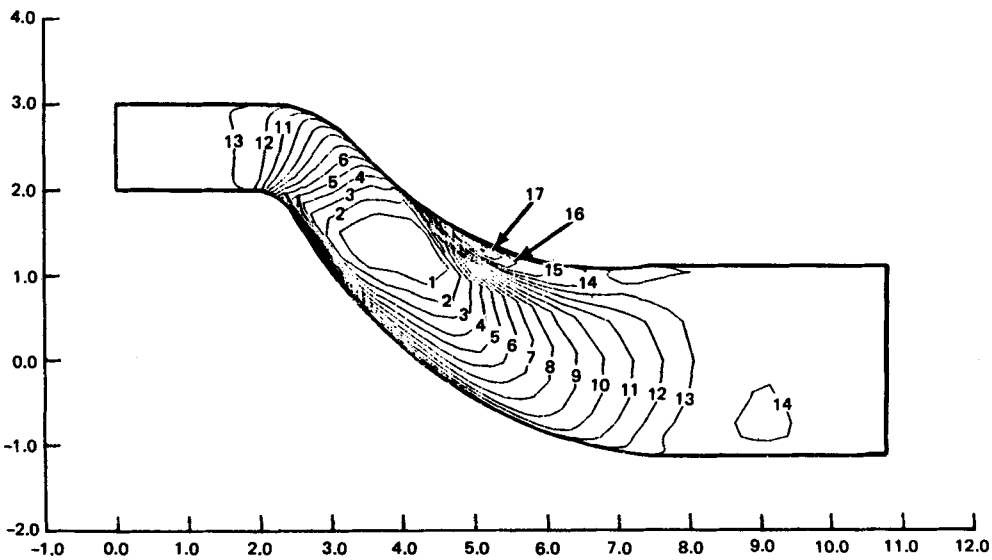

Figure 5. *W*-contours (dimensionless) in symmetry plane

CONTOUR NO.	C_p	CONTOUR NO.	C_p	CONTOUR NO.	C_p	CONTOUR NO.	C_p
1	-1.0553	6	-.5034	11	.0485	16	.6004
2	-.9449	7	-.3930	12	.1589	17	.7108
3	-.8346	8	-.2827	13	.2693	18	.8212
4	-.7242	9	-.1723	14	.3796	19	.9316
5	-.6138	10	-.0619	15	.4900	20	1.0419

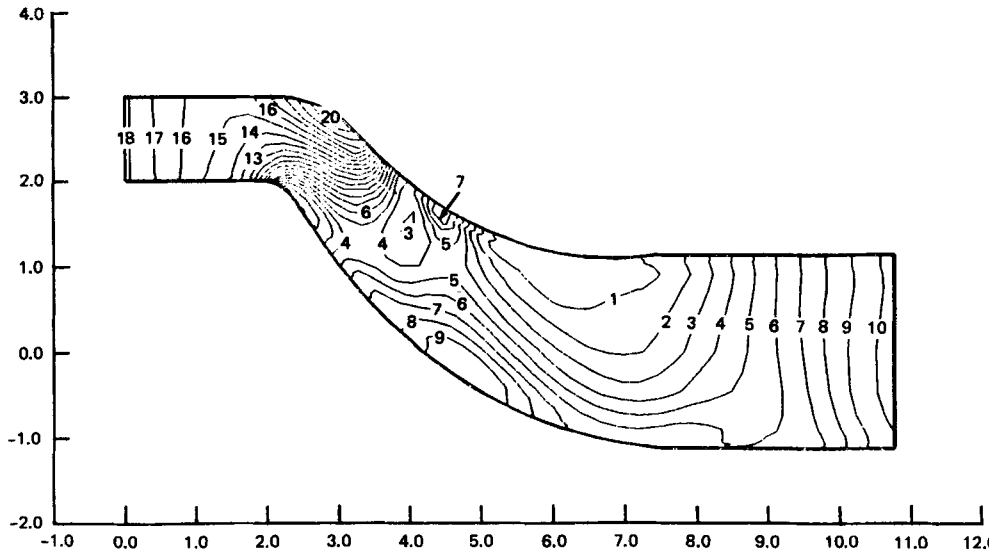

Figure 6. Static pressure contours (dimensionless) in symmetry plane

CONTOUR NO.	DENSITY	CONTOUR NO.	DENSITY	CONTOUR NO.	DENSITY	CONTOUR NO.	DENSITY
1	.1880	6	.3238	11	.4593	16	.5947
2	.2154	7	.3509	12	.4864	17	.6218
3	.2425	8	.3780	13	.5135	18	.6489
4	.2696	9	.4051	14	.5405	19	.6760
5	.2967	10	.4322	15	.5676	20	.7031

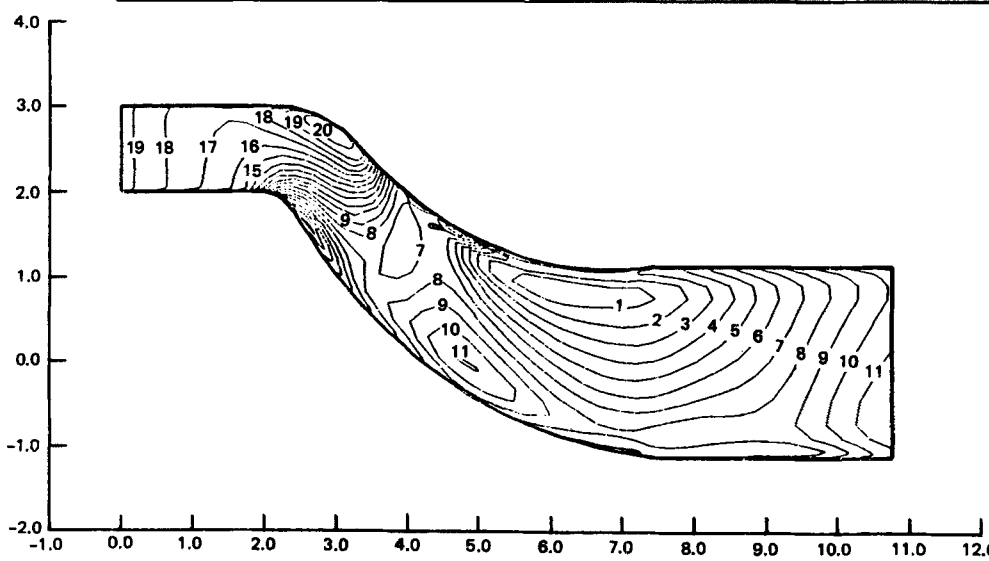

Figure 7. Density contours (dimensionless) in symmetry plane

sectional plots which show the variation of flow properties in planes perpendicular to the channel centreline.

The computational grid in such a transverse plane is shown in Figure 8. Since symmetry exists about a vertical plane through the centreline, only one half of the total cross-section is shown. The co-ordinate grids have been suitably stretched to provide fine spacing near the walls to resolve the turbulent boundary layer structure.

The distribution of axial velocity U in two transverse planes is shown in Figures 9(a) and 9(b). Figure 9(a) is for an axial position just at the end of the second diffuser bend ($J = 32$), while Figure 9(b) is for the exit plane ($J = 46$). In both Figures 9(a) and 9(b) the contour lines for $U = 0$ can be easily estimated—this is the boundary of the separated flow. The separated region is much larger for the upstream location of Figure 9(a). For both locations the separated regions are seen to extend across the entire width of the diffuser. In fact the axial flow appears to be almost two-dimensional over 75–80% of the cross-sectional width in both Figures 9(a) and 9(b).

Figures 10(a) and 10(b) show the distribution of isobars (static pressure) over the same two cross-sectional planes considered in Figures 9(a) and 9(b), namely, the planes at $J = 32$ and $J = 46$ respectively. The pressure distribution in Figure 10(a) is typical of that which occurs when centrifugal forces are significant. The pressure field opposes and approximately balances the centrifugal forces in the interior region away from the diffuser walls. Near the walls, where the longitudinal velocity and hence the centrifugal force are less, the pressure field acts to return the secondary flow to satisfy continuity. For the cross-sectional plane at $J = 46$ (Figure 10(b)) there is no curvature of the duct in the main streamwise direction and therefore no centrifugal force. The static pressure field is now entirely different and the pressure is much more uniform over the cross-section. This greater uniformity can be seen from the fact that the values of the

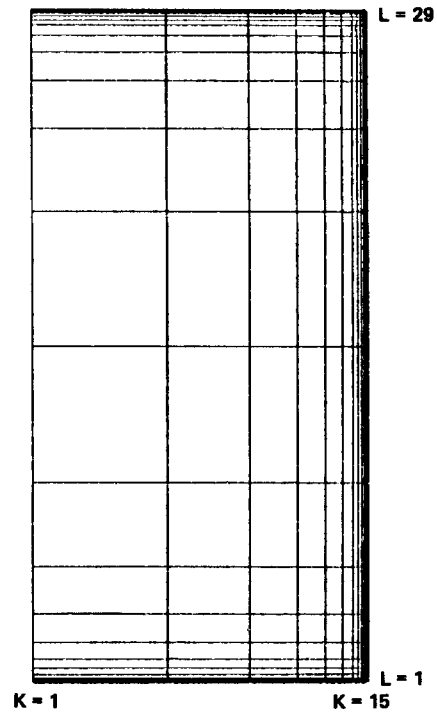

Figure 8. Computational grid in a transverse plane

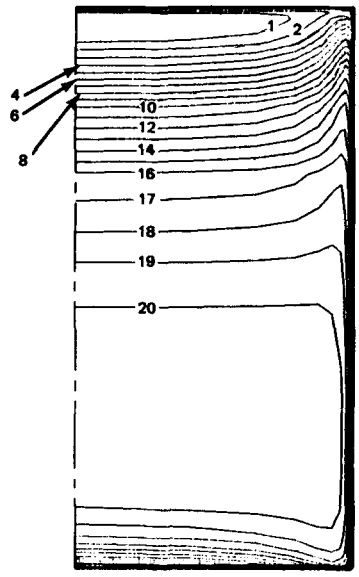

a) J = 32

CONTOUR NO.	U	CONTOUR NO.	U	CONTOUR NO.	U	CONTOUR NO.	U
1	-.7886	6	-.2696	11	.2473	16	.7643
2	-.6832	7	-.1662	12	.3507	17	.8677
3	-.5798	8	-.0628	13	.4541	18	.9711
4	-.4764	9	.0406	14	.5575	19	1.0745
5	-.3730	10	.1440	15	.6609	20	1.1779

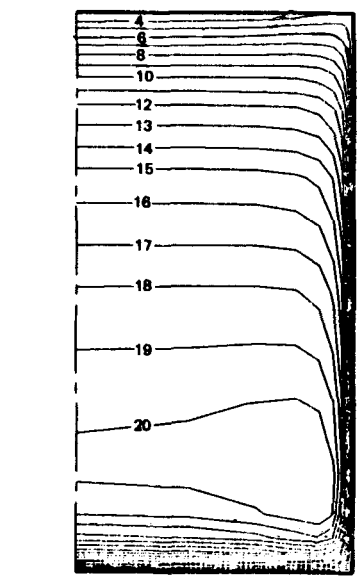

b) J = 46

CONTOUR NO.	U	CONTOUR NO.	U	CONTOUR NO.	U	CONTOUR NO.	U
1	-.2869	6	.0085	11	.3039	16	.5992
2	-.2278	7	.0676	12	.3629	17	.6583
3	-.1687	8	.1266	13	.4220	18	.7174
4	-.1097	9	.1857	14	.4811	19	.7765
5	-.0506	10	.2448	15	.5402	20	.8355

Figure 9. U-contours (dimensionless) in transverse plane for $J = 32, 46$

isobars in Figure 10(a) vary from 0·165 to 0·305 while in Figure 10(b) the variation is only from 0·386 to 0·403. The lack of smoothness of the contour lines in Figure 10(b) is probably caused by numerical error arising from the very small static pressure differences between successive contour lines.

The stretched co-ordinate grid in the transverse plane, shown in Figure 8, is quite coarse in the interior region. The use of such a coarse grid is justified in part by the results shown in Figures 9

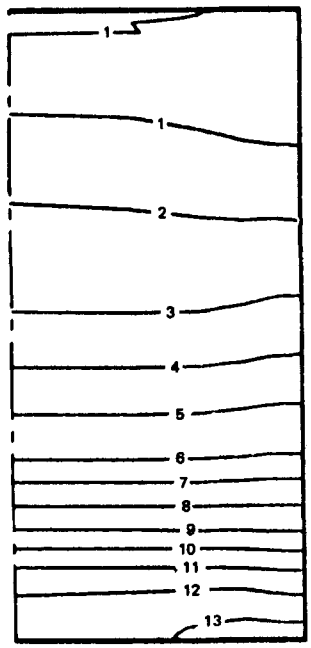

a) J = 32

CONTOUR NO.	C_p	CONTOUR NO.	C_p	CONTOUR NO.	C_p
1	-1.0292	6	-.7719	11	-.5146
2	-.9777	7	-.7204	12	-.4631
3	-.9262	8	-.6690	13	-.4117
4	-.8748	9	-.6175		
5	-.8233	10	-.5660		

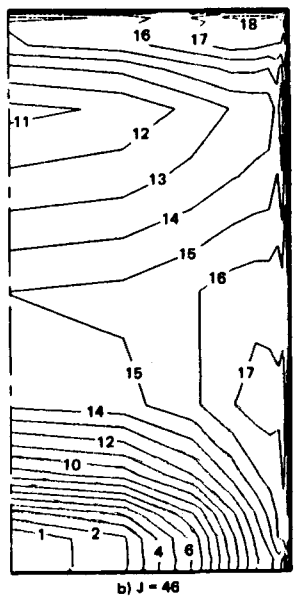

b) J = 46

CONTOUR NO.	C_p	CONTOUR NO.	C_p	CONTOUR NO.	C_p	CONTOUR NO.	C_p
1	-.0617	6	-.0419	11	-.0221	16	-.0024
2	-.0578	7	-.0380	12	-.0182	17	.0016
3	-.0538	8	-.0340	13	-.0142	18	.0056
4	-.0499	9	-.0301	14	-.0103		
5	-.0459	10	-.0261	15	-.0063		

Figure 10. Static pressure contours (dimensionless) in transverse plane for $J = 32, 46$

and 10. In general the velocity and pressure variations exhibited in these figures are greatest near the walls.

Secondary velocity vectors in two cross-sectional planes are shown in Figures 11(a) and 11(b). Again the two cross-sectional planes are located at $J = 32$ and at $J = 46$. A recirculating vortex-type flow can be seen near the top of the diffuser in Figure 11(a). Figure 3 indicates that this

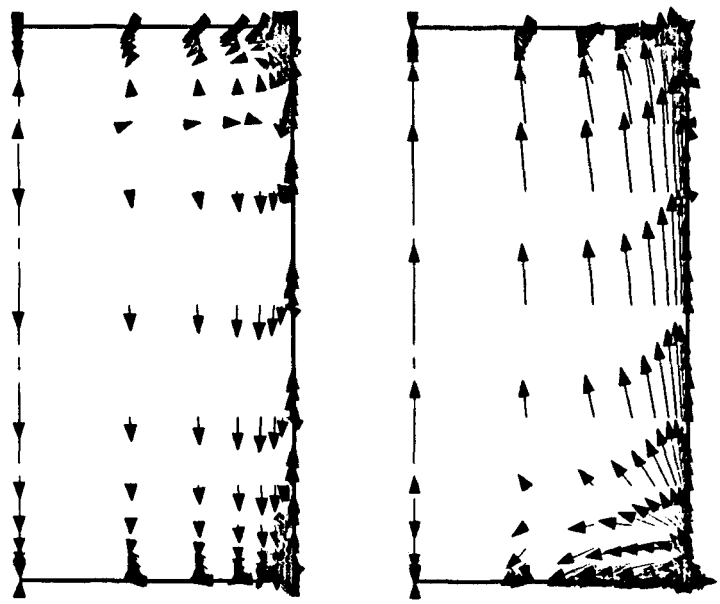

Figure 11. Secondary velocity patterns in transverse plane for $J = 32, 46$

recirculation is occurring within a separated flow region. The secondary flow in the exit plane in Figure 11(b) is not of the recirculating type, but is mainly from the lower to the upper portion of the diffuser. This description is consistent with the exit plane velocity vectors shown in Figure 2. It is noteworthy that the magnitudes of the secondary flow velocities have not been reduced by the length of straight exit pipe as might have been expected, but have actually increased (compare Figures 11(a) and 11(b)).

Convergence to our final results required about 2700 time steps or 11 hours of CPU time on our CRAY-1M computer. About 1·5 M byte central memory storage was needed out of the 2·0 M byte maximum in the CRAY-1M MOS memory. The front end of the system was an IBM 3091. The averaged residuals were reduced by about two orders of magnitude during the computations, as shown in Figure 12.

One of the difficulties of using the present code is the need to assign a value to the exit pressure. A value of 0·4 for the exit static pressure divided by the entrance stagnation pressure was found to produce viable solutions. The estimate of 0·4 was obtained from empirical values for the total pressure loss through a diffuser and through the two turns of the offset diffuser. Using higher values of the exit pressure, e.g., 0·8 and 0·9, resulted in the entire flow degenerating to zero velocity near the diffuser exit.

CONCLUDING REMARKS

This paper indicates that the Thomas code yields useful results for one type of complex, subsonic, internal turbulent flow, even though appreciable separated flow is present. The graphical presentations of pressure and velocity results indicate that the centrifugal, viscous and pressure forces have produced a very complicated three-dimensional flow field. Analysis of the flow by conventional boundary layer techniques would probably be impossible. The computer time requirements of the present code are very large; however, this drawback may be eliminated if the code is vectorized.

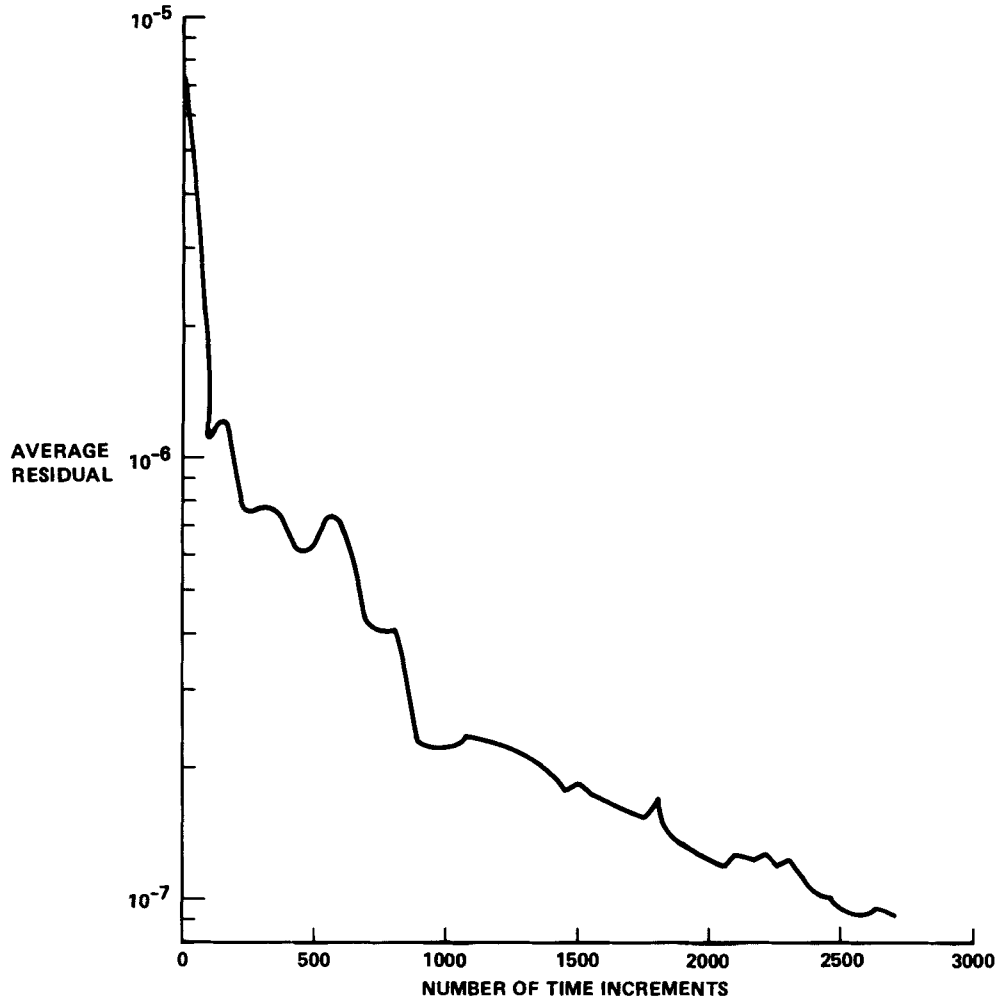

Figure 12. Average residual versus number of time increments

The large extent of one of the separated flow regions would suggest an examination of the validity of the Baldwin–Lomax turbulence model used in this code, but such an examination has not been done here. The turbulence model used here is of the simplest type, the zero equation or algebraic eddy viscosity model. Investigations of the appropriate turbulence models to be used in specific types of flows with flow separation, streamline curvature, rotation and/or shock interaction have recently been carried out.[8,9] Reference 9 concludes that, at least for external flows, the algebraic turbulence model produces results inferior to those based on higher-order models. This conclusion was reached on the basis of a critical comparison of theoretical results with various experimental data.

ACKNOWLEDGEMENTS

A number of my associates made noteworthy contributions to this work. Dr. Michael Siclari was very helpful in making the code operational and also in supplying me with the plotting routines. Dr. John Steinhoff (now Associate Professor at University of Tennessee Space Institute)

originally supplied me with a copy of the code and also was of great help in the initial operation. George Esposito was most adept at tailoring the code to our computers. Kenneth Foreman's continual encouragement and advice made the final paper a reality.

REFERENCES

1. J. N. Scott, 'Numerical solution of the Navier–Stokes equations for 3-D internal flows—An emerging capability', *AGARD Lecture Series No. 140*, 1985, pp. 7-1–7-24.
2. C. E. Towne, 'Application of computational fluid dynamics to complex inlet ducts', *AIAA SAE/ASME/ASEE 21st Joint Propulsion Conf.*, Monterey, CA, 8–10 July 1985, *AIAA Paper 85-1213.*
3. P. D. Thomas *et al.*, 'User's guide for the NOZL3D and NOZLIC computer programs', *NASA CR* 159173, December 1983.
4. P. D. Thomas, 'Numerical method for predicting flow characteristics and performance of nonaxisymmetric nozzles—Theory', *NASA CR 3147*, September 1979.
5. P. D. Thomas, 'Numerical method for predicting flow characteristics and performance of nonaxisymmetric nozzles, Part 2—Application', *NASA CR 3264*, October 1980.
6. R. M. Beam and R. F. Warming, 'An implicit factored scheme for the compressible Navier–Stokes equations', *AIAA J.*, **16** (4), 393–402 (1978).
7. B. S. Baldwin and H. Lomax, 'Thin layer approximation and algebraic model for separated turbulent flows', *AIAA paper 78-257*, January 1978.
8. B. Lakshminarayana, 'Tubulence modeling for complex flows', *AIAA paper 85-1652*, July 1985.
9. J. G. Marvin, 'Turbulence modeling for computational Aerodynamics', *AIAA J.*, **21** (7), 941–955 (1983).